Shapes of Langmuir Monolayer Domains in Confined Geometries

Z. Khattari and Th. M. Fischer*

Max Planck Institut of Colloids and Interfaces, Am Mühlenberg 1, 14476 Golm, Germany

Received: June 5, 2001; In Final Form: September 17, 2001

The shape of two-dimensional liquid expanded droplets of a methyl octadecanoate Langmuir monolayer confined in gas cavities in a liquid condensed matrix is studied using fluorescence microscopy. Confinement destabilizes the circular shape by increasing the dipole density of the liquid expanded phase or by decreasing the bare line tension λ between the liquid expanded and the gaseous phase. Confinement causes a cascade of shape transitions from a circular droplet toward shapes of n-fold symmetry with increasing n until the droplet returns to a circle as its size approaches the size of the cavity. The experiments are explained theoretically, and it is shown that the three phase coexistence region is not an equilibrium phase coexistence region. Material parameters depend on the relative area fraction of the coexisting phases.

I. Introduction

Confining liquids to small cavities changes the behavior of the liquid if the size of the cavity is in the range of the dominating interactions. One of the most prominent effects of confinement is a crossover from a continuum mean field behavior on a large length scale to a behavior where steric interactions between individual molecules become important. Experiments on simple liquids with the surface force apparatus show continuum Derjaguin Landau Verwey Overbeek (DLVO) forces[1,2] at large distances[3] and oscillatory interactions at short distances.[4] A layering of the molecules at surfaces with an increase of the liquid viscosity and the appearance of a yield stress on confinement has been observed.[5] The typical length scale of interactions causing the glass transition of three-dimensional liquids[6] could be measured by confining the liquid in nanopores. However, a change of behavior on confinement is not limited to confinement on molecular length scales. Water placed between hydrophobic solid surfaces causes attraction between the surfaces, which are much stronger than expected by continuum (DLVO) theories.[7] The onset of these confinement effects is an apparent enhancement of the interaction strength, compared to the unconfined situation. Casimir forces,[8] caused by a change of the spectrum of thermal fluctuations upon confinement, also are of long-range nature with an algebraic dependence on the length scale of the confinement.

Length scales of simple 3d liquids are in the nanometer range, and it is difficult to visualize the dynamic structure on this length scale. In contrast, electrostatic interactions of 2d liquids residing at an interface between two 3d liquids are long-range interactions. For example, Langmuir monolayers at the air/water interface exhibit peculiar patterns in phase coexistence regions,[9] which are in the range of 100 microns. Those patterns have successfully been described by the competition of intermolecular dipole interactions and the line tension acting at the phase boundaries. Among the patterns, transitions of unconfined microdroplets from circular to n-fold symmetric shapes have been observed as a function of the monolayer composition.[10]

Here we report on the effect of confinement on the shape of liquid expanded Langmuir monolayer droplets. Liquid expanded droplets are confined in 2d circular microgas cavities of a liquid condensed matrix and forced to undergo shape transitions by reducing the gas cavity radius. The boundary conditions imposed on the droplets by confining them into the cavities causes two effects. The liquid condensed matrix can be considered as a solid phase, such that flow of the monolayer is allowed only in the interior of the cavity. The liquid condensed phase has a density of electric dipoles, which differs from the liquid and the gaseous phase. The presence of the dipoles within the liquid condensed phase gives rise to an electrostatic potential. Both the effect of the hydrodynamic boundary condition and the electrostatic cavity potential on the stability of the droplet shape are calculated theoretically in the following two sections. The experiments with confined droplets are presented in section IV. They are compared with the theory in section V, and it is shown that as for 3d liquids the material parameters of 2d liquids such as the dipole densities and line tensions change upon confinement. A summary of the results is listed in the conclusions.

II. Hydrodynamics in Confined Cavities

Consider a 2d liquid droplet slightly distorted from a circular (radius R) shape and confined in the center of a 2d cavity of radius B (Figure 1). The monolayer material outside the radius B is considered as solid, whereas both the gaseous and the liquid expanded phase are 2d fluids of negligible surface shear viscosity.[11] Viscous dissipation therefore is governed by the flow of the 3d subphase under the monolayer. A positive effective line tension λ_{eff} between the liquid and gaseous phase will force the deformed shape back to a circle thereby causing flow within the liquid expanded and gaseous phase and the subphase. In the present section, we will derive an expression for the dynamics of a harmonic distortion of the form

$$r_{\mathrm{d}}(\vartheta,t) = R\left[1 + \sum_n \epsilon_n(t)\cos(n\vartheta) - \sum_n \frac{\epsilon_n^{\,2}(t)}{4}\right] \qquad (1)$$

where $r_{\mathrm{d}}(\vartheta,t)$ denotes the time dependent deformed shape in polar coordinates r and ϑ and $\epsilon_n(t) \ll 1$ is a dimensionless measure of the distortion of the nth harmonic mode. The last

* To whom correspondence should be addressed. E-mail: thomas.fischer@mpikg-golm.mpg.de.

10.1021/jp0121419 CCC: $22.00
Published on Web 01/29/2002

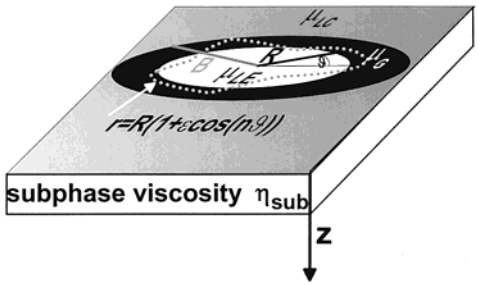

Figure 1. Liquid expanded domain of radius R and dipole density μ_{LE} suspended into a two-dimensional incompressible gaseous cavity (dipole density μ_G) within a liquid condensed monolayer matrix (dipole density μ_{LC}). The two-dimensional flow of the liquid expanded domain and the gas cavity is coupled to a three-dimensional fluid (subphase) of viscosity η_{sub}. A distortion described by eq 1 (dotted line) is sketched.

term in (1) ensures that the area of the droplet is conserved to the order ϵ^2 during the distortion. The hydrodynamics of unconfined droplets has been evaluated by Stone and McConnell,[12] and we closely follow their analysis. The flow of the subphase is described by Stokes equations and the continuity equation

$$-\nabla p + \eta\nabla^2\mathbf{u} = 0 \quad \text{and} \quad \nabla\cdot\mathbf{u} = 0 \tag{2}$$

where p is the subphase pressure and $\mathbf{u}$ denotes the subphase velocity. The general solution in a cylindrical coordinate system (r,ϑ,z) can be written as[13]

$$\mathbf{u} = \nabla\Xi + \nabla\times(\mathbf{e}_z\Psi) + r\frac{\partial}{\partial r}(\nabla\Pi) + \mathbf{e}_z\frac{\partial\Pi}{\partial z} \quad \text{and}$$

$$p = -2\eta\frac{\partial^2\Pi}{\partial z^2} \tag{3}$$

where Ξ,Ψ, and Π are scalar functions solving the Laplace equation

$$\nabla^2\{\Xi,\Psi,\Pi\} = \{0,0,0\} \tag{4}$$

From the velocity boundary conditions $u_z(z=0)=0$ and from the incompressibility of all monolayer phases $\nabla_s\cdot u_s = 0$ (∇_s and $\mathbf{u}_s$ are the surface gradient and the surface velocity), it follows that $\Pi = \Xi = 0$ and all streamlines are lying in planes parallel to the air/water interface. The remaining stream function Ψ which is in accordance with the harmonic distortion eq 1 is

$$\Psi(r,\vartheta,z) = 2\sin n\vartheta\int_0^\infty \mathrm{d}k\, k^{-1}a(k)J_n(kr)\mathrm{e}^{-kz}, \tag{5}$$

where $a(k)$ is a function of k to be determined and $J_n(kr)$ is the Bessel function of order n and argument kr. Using eqs 5 and 3 we find

$$u_r(r,\vartheta,z) = \cos n\vartheta\int_0^\infty \mathrm{d}k\, a(k)[J_{n+1}(kr) + J_{n-1}(kr)]\mathrm{e}^{-kz}$$

$$u_\vartheta(r,\vartheta,z) = \sin n\vartheta\int_0^\infty \mathrm{d}k\, a(k)[J_{n+1}(kr) - J_{n-1}(kr)]\mathrm{e}^{-kz}$$

$$u_z(r,\vartheta,z) = 0$$

$$p(r,\vartheta,z) = \text{constant} \tag{6}$$

The fluid motion of the liquid expanded and gaseous phase obey the 2d-Stokes equation:

$$\left(-\nabla_s\pi_m + \eta\frac{\partial\mathbf{u}}{\partial z}\right)_s + \mathbf{n}(\vartheta)\lambda_{eff}(n)\kappa(\vartheta)\delta(r - r_d(\vartheta)) = 0 \quad \text{for} \quad r < B,\ z = 0 \tag{7}$$

Here π_m is the surface pressure of the monolayer, ∇_s is the surface gradient, the second term is the viscous drag force from the subphase, and the last term ensures that the dynamic normal surface stress satisfies the Laplace condition. $\mathbf{n}$ is the inward normal vector to the boundary of the droplet, $\lambda_{eff}(n)$ is the effective line tension, and $\kappa(\vartheta)$ is the curvature of the liquid-expanded/gaseous interface. For r larger than B, the monolayer is solid requiring

$$\mathbf{u}_s = 0 \quad \text{for} \quad r > B,\ z = 0 \tag{8}$$

Expansion of the last term in (7) until terms linear in ϵ_n, taking the surface curl, which eliminates the surface pressure, and insertion of eq 6 leads to the integral equation for $a(k)$:

$$\int_0^\infty \mathrm{d}k\, 2\eta k^2 a(k)J_n(kr) = \epsilon_n(t)\frac{n\lambda_{eff}(n)}{r^2}(n^2-1)\delta(r-R) \quad \text{for} \quad r < B \tag{9}$$

Two additional integral equations are obtained when inserting eq 6 into eq 8:

$$\int_0^\infty \mathrm{d}k\, a(k)J_{n\pm1}(kr) = 0 \quad \text{for} \quad r > B \tag{10}$$

This set of equations can be solved by expanding $a(k)$ into a series of Bessel functions:

$$a(k) := (kB)^{-1/2}\sum_{m=0}^{\infty}\alpha_m J_{n+2m+5/2}(kB) \tag{11}$$

The expansion (11) automatically satisfies eq 10. Applying the relation[14]

$$(kB)^{-5/2}J_{n+2m'+5/2}(kB) =$$

$$\frac{1}{B}\int_0^B \mathrm{d}r\left(\frac{r}{B}\right)^n\left(1-\frac{r^2}{B^2}\right)^{3/2}\frac{\Gamma(n+m'+1)}{2^{3/2}\Gamma(m'+5/2)\Gamma(n+1)}\times$$

$${}_2F_1\left(-m',n+m'+5/2,n+1,\frac{r^2}{B^2}\right)J_n(kr) \tag{12}$$

to eq 9 and inserting the expansion (11) leads to the result

$$\alpha_m = -\epsilon_n(t)\frac{n(n^2-1)\lambda_{eff}(n)}{\eta}(n+2m+5/2)\times$$

$$\frac{\Gamma(n+m+1)}{2^{3/2}\Gamma(m+5/2)\Gamma(n+1)}\left(\frac{R}{B}\right)^{n-1}\left(1-\frac{R^2}{B^2}\right)^{3/2}\times$$

$${}_2F_1\left(-m,n+m+5/2,n+1,\frac{R^2}{B^2}\right) \tag{13}$$

where ${}_2F_1$ is the hypergeometric function. The solution can be completed by requiring that the flow velocity at the droplet boundary must coincide with the velocity of the boundary:

$$u_r(R,\vartheta,0) = R\dot{\epsilon}_n(t)\cos n\vartheta \tag{14}$$

with $\dot{\epsilon}_n = \mathrm{d}\epsilon_n/\mathrm{d}t$, which leads to the equation

$$\dot{\epsilon}_n(t) = -\gamma_n^c\epsilon_n(t) \tag{15}$$

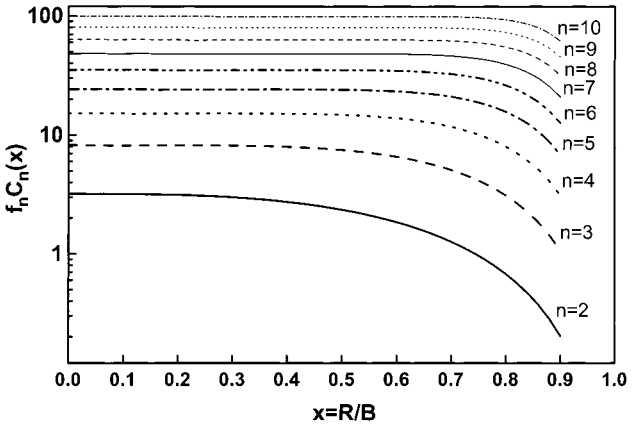

Figure 2. Plot of the confined mobility $f_nC_n(x)$, $n = 2-10$ (eqs 17 and 18) as a function of the confinement $x = R/B$. Below $x < 0.5$, the droplet can be considered as unconfined. Confinement decreases the mobility especially for the harmonic distortions with lower n as x approaches 1.

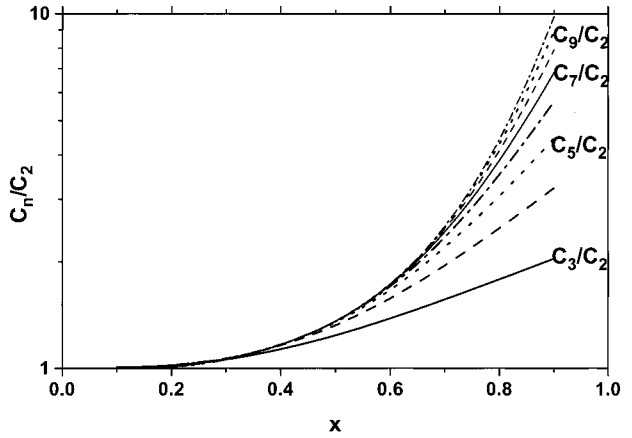

Figure 3. Plot of $C_n(x)/C_2(x)$, $n = 2-10$ showing that higher harmonic modes are relatively more mobile than lower modes when the droplet is confined.

with the confined relaxation rate

$$\gamma_n^{\,c} = \frac{\lambda_{\text{eff}}(n)}{\eta\pi R^2} f_n C_n\left(\frac{R}{B}\right) \tag{16}$$

where

$$f_n = \frac{4n^2(n^2-1)}{4n^2-1} \tag{17}$$

is the unconfined dimensionless viscous mobility coefficient of the nth mode[12] and the function $C_n(x)$

$$C_n(x) = \frac{(4n^2-1)\pi}{16}\sum_{m=0}^{\infty}(n+2m+5/2)x^{2n-1}(1-x^2)^3 \times \left[\frac{\Gamma(n+m+1)}{\Gamma(m+5/2)\Gamma(n+1)}{}_2F_1(-m,n+m+5/2,n+1,x^2)\right]^2 \tag{18}$$

describes the effect of the confinement. In Figure 2, we plot the confined viscous mobility coefficient $f_nC_n(x)$ as a function of the confinement $x = R/B$. Confinement of the droplet reduces the relaxation rate as B approaches R. It is important for $x > {}^1/_2$ for mode 2. For higher modes, the effects of confinement become important for x values closer to $x = 1$ than for lower modes. In Figure 3, the hydrodynamic effect of the confinement on the ratio $C_n(x)/C_2(x)$ is shown. For the unconfined droplets and large n, the mobility is proportional to $f_n \propto n^2$, whereas for the confined droplets, it increases as n^β with $\beta > 2$. Higher modes decay faster than the lower modes if the droplet is confined.

III. Electrostatics and Effective Line Tension of Confined Droplets

The surfactants forming a Langmuir monolayer are aligned asymmetrically at the air/water interface, and therefore, all phases consist of electrical dipoles normal to the air/water surface. The dipoles give rise to a dipole density or surface potential ΔV across the interface, which we characterize by the parameter μ defined via

$$\mu = \sqrt{\frac{\epsilon_0}{4\pi}\frac{2\epsilon_w\epsilon_{\text{air}}}{\epsilon_w+\epsilon_{\text{air}}}}\Delta V \tag{19}$$

The vacuum permittivity is denoted by $\epsilon_0 = 8.85$ pN/V^2, and ϵ_{air} (ϵ_w) is the relative permittivity of air (water). In the present problem, three monolayer phases each with a different value for μ (μ_{LC}, μ_{G}, and μ_{LE}, see Figure 1) are involved. Only the differences in μ from one phase to the other play a role, and we will use the two parameters $\mu_{\text{LE/G}} = \mu_{\text{LE}} - \mu_{\text{G}}$ and $\mu_{\text{LC/G}} = \mu_{\text{LE}} - \mu_{\text{G}}$. Electrostatic interactions are important at distances beyond the molecular scale, whereas at molecular distances, other interactions such as van der Waals attraction and steric repulsion dominate. As we are interested in phenomena on a mesoscopic scale, the short range interactions are sufficiently well described by cutting off the dipolar interactions at molecular distances Δ. If different phases of different dipole density coexist, the total energy can be described by the sum of line tension and electrostatic energies:

$$W = \sum_{f_{ij}}\int_{f_{ij}}(\lambda_{ij}-\mu_{ij})\,\mathrm{d}s - \frac{1}{2}\sum_{f_{ij},f_{kl}}\mu_{ij}\mu_{kl}\iint_{f_{ij},f_{kl}}\frac{\mathrm{d}s\mathrm{d}s'}{\sqrt{(\mathbf{r}(s)-\mathrm{r}(s'))^2+\Delta^2}} \tag{20}$$

Here λ_{ij} is the bare line tension, and μ_{ij} is the difference in μ between phases i and j. The facette between phases i and j is denoted by f_{ij} and ds is a line element attached to the facette at point $\mathbf{r}(s)$. The effect of electrostatic interactions is to renormalize the bare line tension λ. The effective line tension $\lambda_{\text{eff}} < \lambda$ defined via

$$\lambda_{\text{eff}}[\mathbf{r}(s),\delta\mathbf{r}(s)] = \left(\frac{\delta W}{\delta P}\right)_A \tag{21}$$

is not a materials parameter. In contrast to the bare line tension λ, it depends on the area A, the shape $\mathbf{r}(s)$, and the mode of deformation $\delta\mathbf{r}(s)$ of the domain with perimeter P. Working out λ_{eff} in eq 21 with the deformation of the form (1) leads to the result

$$\lambda_{\text{eff}}(n) = -\,\mu_{\text{LE/G}}{}^2\ln\frac{R}{R_n^{\,c}} \tag{22}$$

where

$$R_n^{\,c} = R_n^{\,*}\exp\left[\frac{\mu_{\text{LC/G}}}{\mu_{\text{LE/G}}}\frac{1}{n^2-1}\Lambda\left(\frac{R}{B}\right)\right] \tag{23}$$

and[10,15,16]

$$R_n = \frac{\Delta}{8} e^{\lambda/\mu_{LE/G}^2} e^{Z_n} \tag{24}$$

are the radii of the confined and unconfined droplet where the circular shape gets unstable with respect to an n-fold deformation. The numbers Z_n are[15]

$$Z_n = 1 + \frac{n^2}{3}\sum_{k=0}^{n-2}\frac{1}{k!}\prod_{j=0}^{k-1}\frac{(1+j)^2(2-n+j)(2+n+j)}{(3/2+j)(5/2+j)(3+j)} = 1 + \frac{n^2}{3}{}_4F_3\left(1,1,2-n,2+n;\frac{3}{2},\frac{5}{2},3;1\right) \tag{25}$$

The effect of the confinement is described by (see the Appendix)

$$\Lambda(x) = 4x\frac{(1+x^2)E(x) - (1-x^2)K(x)}{(1-x^2)^2} \tag{26}$$

where

$$0 < x = R/B < 1; \quad K(k) := \int_0^{\pi/2}\frac{d\vartheta}{\sqrt{1-k^2\sin^2\vartheta}}$$

and

$$E(k) := \int_0^{\pi/2}\sqrt{1-k^2\sin^2\vartheta}\,d\vartheta$$

are the complete elliptic integrals of the first and second kind. For methyl octadecanoate, which is investigated experimentally in the current work, it is[17] $\lambda_{LE/G} = 0.5 \pm 0.3$ pN,[18] $\Delta \approx 1$ nm, $\mu_{LE/G}^2 = 0.025 \pm 0.01$ pN, and $\mu_{LC/G}^2 = 0.1 \pm 0.05$ pN.[19] Using these values, we find that $\lambda_{eff}(n) > 0$ for all modes n and the circular droplet shape is stable. For an unstable shape, we have to assume that some of the material parameters change as the droplet is confined. In Figure 4, we plot the effective line tension $\lambda_{eff}(n)$ for $n = 2-25$ at fixed $R = 12$ μm as a function of x,B, respectively, assuming a lower bare line tension of $\lambda_{LE/G} = 0.17$ pN.[20] The effective line tension increases as the droplet is confined into smaller and smaller cavities. Confinement stabilizes the circular droplet shape. Above a confinement of $x > 0.9$ ($B < 13.3$ μm), all modes unstable for the unconfined droplet are stable. The stabilizing effect is stronger for the lower and weaker for the higher deformation modes. For the unconfined droplet, one has $\lambda_{eff}(n) < \lambda_{eff}(n+1)$ and the tension is lowest for an ellipsoidal deformation. Confining the droplet alters this sequence. Above a critical confinement $x > x_{n,n+1}$, the $(n+1)$th mode is less stable than the nth mode. The critical confinement $x_{n,n+1}$ is given by the implicit equation

$$\frac{2n+1}{(n-1)n(n+1)(n+2)(Z_{n+1}-Z_n)}\Lambda(x_{n,n+1}) = \frac{\mu_{LE/G}}{\mu_{LC/G}} \tag{27}$$

and depends on the relative ratio of the dipole density difference of the droplet and the confining phase. In Figure 5, we plot a phase diagram showing the regions in the $x - \mu_{LE/G}/\mu_{LC/G}$ plane, where the nth mode has the lowest tension. Lower modes are less stable for small x and large $\mu_{LE/G}/\mu_{LC/G}$. The opposite is true for higher modes. For $\mu_{LE/G}/\mu_{LC/G} = 1/2$, we find $x_{2,3} = 0.4$, $x_{3,4} = 0.5$, $x_{4,5} = 0.58$, $x_{5,6} = 0.64$, etc.

In the interval $x_{n-1,n} < x < x_{n,n+1}$, the circular droplet is unstable if $\lambda_{eff}(n) < 0$. The droplet can be made unstable by increasing R, B, or $\mu_{LE/G}$ or decreasing λ or $\mu_{LC/G}$. The shape of the droplet does not necessarily assume a deformation with the mode n but is determined by the fastest growing mode. The confined mobility coefficient $f_nC_n(x) > 0$ increases with increasing n (see Figure 2). Hence, if $\lambda_{eff}(n) < 0$, then the fastest growing unstable mode in the interval $x_{n-1,n} < x < x_{n,n+1}$ is of a harmonic order equal to or larger than n. The details, which of the mode is the fastest one, depend on the whole set of material parameters λ, Δ, $\mu_{LE/G}$, and $\mu_{LC/G}$ and on the geometry defined by R and B. In Figure 6, we plot γ_n^c $n = 1-30$ as a function of R for $\lambda_{LE/G} = 0.17$ pN, $\Delta \approx 1$ nm, $\mu_{LE/G}^2 = 0.025$ pN, $\mu_{LC/G}^2 = 0.1$ pN, and $B = 22$ μm. The droplet gets unstable with respect to a 2-fold deformation at $R = 1.1$ μm. With increasing R, the minimum relaxation rate shifts to higher n until at $R = 19.8$ μm the 24th mode is the last mode being restabilized. Above $R = 19.8$ μm, the circular droplet is once again stable.

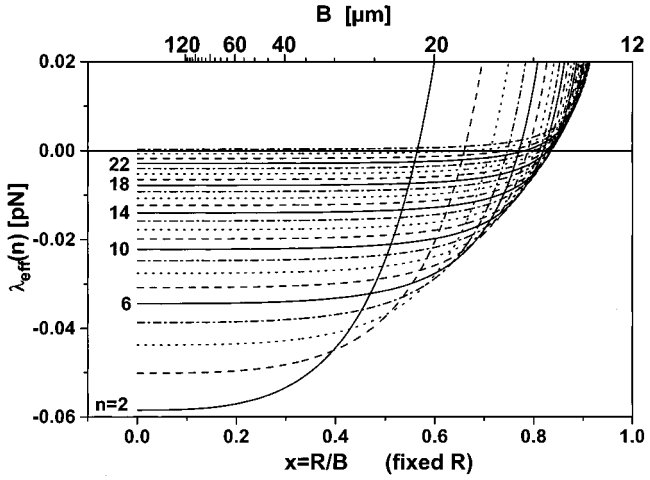

Figure 4. Plot of the effective line tension $\lambda_{eff}(n)$, $n = 2-25$ as a function of $x = R/B$ for $R = 12$ μm, $\lambda = 0.17$ pN, $\Delta \approx 1$ nm, $\mu_{LE/G}^2 = 0.025$ pN, and $\mu_{LC/G}^2 = 0.1$ pN. Decreasing cavity size B increases the effective line tension, which is negative for $n < 25$ and $x = 0$. The sequence of the modes is changed because of the confinement, and at $x = 0.9$, all modes are stable ($\lambda_{eff}(n) > 0$ for all n). Note that at fixed R, λ, $\mu_{LE/G}^2$, and $\mu_{LC/G}^2$ an unconfined droplet which is stable ($\lambda_{eff}(n) > 0$ for all n) remains stable when being confined.

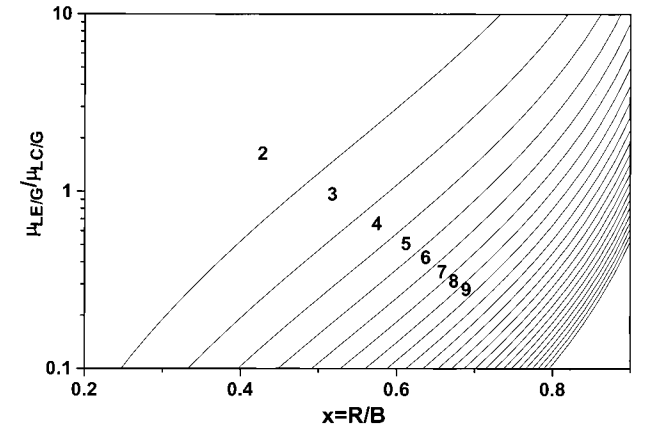

Figure 5. Phase diagram showing the regions in the $x - \mu_{LE/G}/\mu_{LC/G}$ plane where the nth mode is the mode with the lowest effective line tension. Confinement of the droplet or decreasing $\mu_{LE/G}/\mu_{LC/G}$ increases the index of the less stable mode.

IV. Experimental Section

Experiments are performed in methyl octadecanoate in the three phase coexistence regions—liquid condensed (LC), liquid expanded (LE), and gaseous (G)—on pure water ($\Theta = 24$ °C,

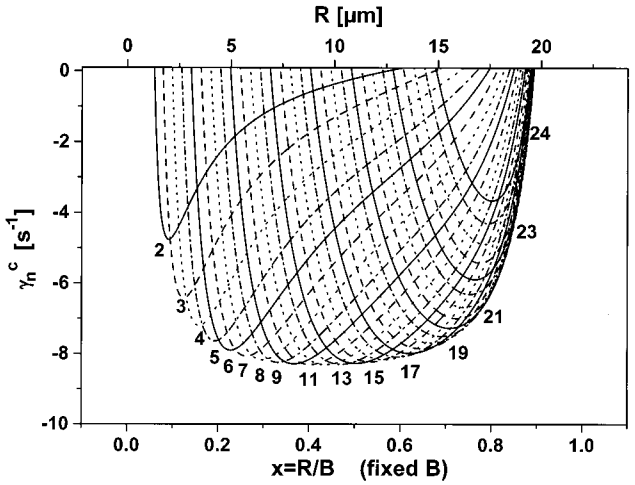

Figure 6. Plot of the confined relaxation rate $\gamma_n c(n)$, $n = 2-30$ as a function of $x = R/B$ for $B = 22$ μm, $\lambda = 0.17$ pN, $\Delta \approx 1$ nm, $\mu_{LE/G}^2 = 0.025$ pN, and $\mu_{LC/G}^2 = 0.1$ pN. Increasing the droplet radius R initially decreases the relaxation rate. The rate changes sign when $\lambda_{eff}(n)$ becomes negative, passes through a minimum, and returns to positive as the electrostatic confinement restabilizes the nth mode. The curves for increasing harmonic mode n are shifted toward higher x, and the index of the fastest growing unstable mode shifts from $n = 2$ toward $n = 24$ as the radius increases from $R = 1.1-19.8$ μm. For $R > 19.8$ μm, all modes are restabilized by the electrostatic confinement.

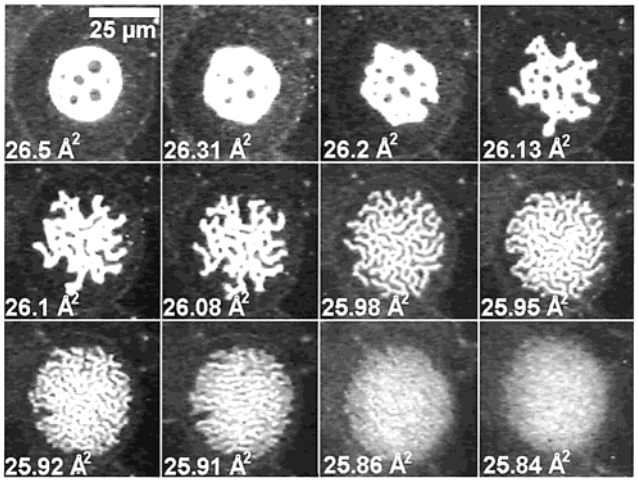

Figure 7. Fluorescence microscopy images of a LE droplet (bright) in a G cavity (dark) within a LC matrix (gray) of a methyl octadecanoate Langmuir monolayer $\Theta = 24$ °C. The shape deformation of the LE droplet occurring upon compression of the monolayer is shown. The deformation mode increases as the droplet is more and more confined until the length scale of the pattern decreases below the resolution of the microscope. At the end of the compression, a less bright droplet of homogeneous LE phase remains.

$\eta = 0.725$ mNs/m^2 [21]). After spreading and compressing the monolayer to an area per molecule of $A_{mol} = 60$ Å^2, the monolayer is heated to a temperature of $\Theta = 32$ °C and left for equilibration. After 30 min, we cool the monolayer to $\Theta = 24$ °C and slowly ($\dot{A}_{mol} = -2.6$ Å^2/min) compress the monolayer. In this way, we can produce extended LC phase incorporating circular G cavities which themselves contain droplets of LE phase. Part of the LE droplets completely dewet the LC/G boundary and are centered in the G cavity. Figure 7 shows a LE droplet (bright) with such a G cavity (dark) immersed into LC surroundings (gray). Initially, at $A_{mol} = 26.5$ Å^2, the cavity radius is about twice the radius of the LE droplet in the cavity. Upon compression, the cavity decreases and assumes an ellipsoidal shape with a maximal ratio of the two axes of 0.88.

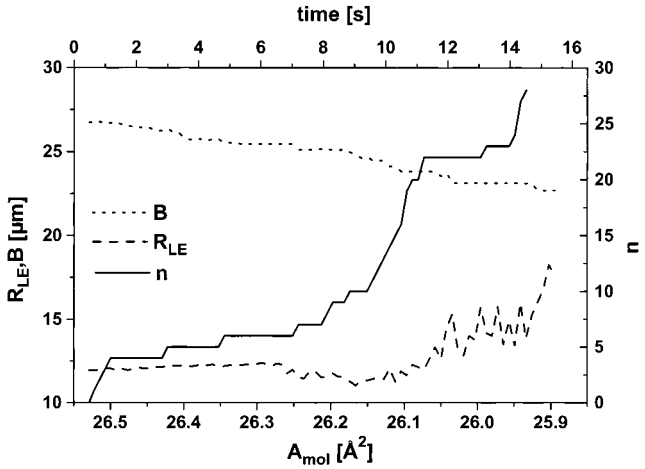

Figure 8. Plot of the compact radius $R_{LE} = (A_{LE}/\pi)^{1/2}$ of the LE droplet, the cavity radius B, and the deformation mode n as a function of time and the area per molecule A_{mol}. Initially no change in the radius of the droplet is detected. The droplet becomes unstable as B decreases. Only after compression to an area per molecule of $A_{mol} = 26.15$ Å^2, the radius of the droplet increases accompanied by a further decrease of B and increase of n.

Initially, also, the LE-droplet area decreases until at $A_{mol} = 26.15$ Å^2 it passes through a minimum and then increases. At $A_{mol} = 26.5$ Å^2, the first shape instability of the LE-droplet shape is observed, and upon compression, it successively assumes shapes of n-fold symmetry with increasing n. Only the first three images in Figure 7 resemble a "slightly distorted circle" which is the basis of the theoretical calculations. All of the other shapes are much more complicated such that agreement between theory and experiment can be expected to be at best qualitative. In Figure 8, the radius B of the boundary, the compact radius $R_{LE} = (A_{LE}/\pi)^{1/2}$ (A_{LE} is the area of the LE droplet), and harmonic mode n (obtained by counting the number of dangling ends of the droplet) are plotted as a function of time and the area per molecule A_{mol}. The droplet becomes unstable at $A_{mol} = 26.5-26.35$ Å^2, whereas B decreases and R is constant. Presumably, the instability occurs on compression of the monolayer because the decrease in B is accompanied with an increase in $\mu_{LE/G}$ or a decrease in $\mu_{LC/G}$ or the bare line tension λ (cf. Figure 5). Further compression of the monolayer converts the G phase into LE and LC such that R increases and B decreases. The increase in n observed in this regime qualitatively follows the scenario predicted for increasing R and fixed B, $\mu_{LE/G}$, $\mu_{LC/G}$, and λ (Figure 6).

LE droplets in other cavities resemble the one shown in Figure 7. However, the values of A_{mol} where the shape transitions occur and where the LE area is minimal vary from droplet to droplet even if the values of B and R are comparable. From the preparation of the monolayer, it is clear that LE droplets in different cavities vary in the amount of fluorescence label dissolved in each droplet. The average surface pressure measured with a Wilhelmy plate is smaller than 1 mN/m in the experiments. Assuming that the LE matrix may sustain surface pressure gradients on the order of μN/m^2, then the surface pressure inside the gas cavities might vary substantially from one cavity to another. From this point of view, the spread of shape transitions from one cavity to the next is not surprising.

V. Discussion

In the experiments, the shape instability occurs on compression of the monolayer, where the confined droplet at least initially preserves its area. If the three phase coexistence region

were an equilibrium phase coexistence region of macroscopically separated phases, then a lever rule should hold and material parameters such as $\mu_{LE/G}$, $\mu_{LC/G}$, the surface pressure π_m, and λ should not depend on the relative area fractions of the three coexisting phases. It is well documented from surface pressure area isotherms that the surface pressure in the coexistence region of two phases is not constant in monolayers. The presented experiment is a proof that the other material parameters $\mu_{LE/G}$, $\mu_{LC/G}$, and λ are not constant either. A shape instability at constant R and decreasing B cannot be explained in the framework of the energy (eq 20) if $\mu_{LE/G}$, $\mu_{LC/G}$, and λ do not change upon compression. The validity of eq 20 has been proven by numerous experiments on monolayer patterns. The compression rate is slow enough to allow for the evolution of noncircular domains. Hence, the effect of the confinement must increase $\mu_{LE/G}$ or to decrease the bare line tension λ. However, it should be mentioned that the linear stability calculation of a slightly distorted circular drop gives a simplified picture of the much more complicated droplet shapes observed in the experiments.

In the second regime, compression converts the G phase into LE and LC and the area of the LE droplet increases, which is accompanied by an increase of the deformation mode n. Although the requirement that the deformation parameter should be small ($\epsilon_n \ll 1$) is no longer fulfilled, the experimental data is in qualitative agreement with the theoretical predictions (see Figures 6 and 8).

The theory predicts that because of the electrostatic confinement the circular shape must become stable again as R approaches B. Unfortunately, the value of n increases too much in the experiment, such that the patterns at $R \approx B$ are below the resolution limit of the fluorescence microscope, and only a blurred gray area within the cavity can be seen (Figure 7, A_{mol} = 25.86 and 25.84 Å^2). AFM experiments with films transferred onto solid supports similar to those performed by Schwartz et al.[22] to unravel the cusp angle of small virtual defects only work for liquid condensed phases not for liquid expanded and gaseous phases.

A quantitative comparison of the experiments with the theory is difficult as the material parameters $\mu_{LE/G}$, $\mu_{LC/G}$, and λ are known only with low precision. Assuming that confinement reduces the bare line tension to about half of the value stated in ref 18 and leaves the other parameters unchanged gives reasonable agreement between theory and experiment.

VI. Conclusions

Confining two-dimensional droplets of the LE phase of a Langmuir monolayer into cavities destabilizes the circular shape by increasing the dipole density of the liquid expanded phase or by decreasing the bare line tension λ between the liquid expanded and the gaseous phase. Circular droplets deform and assume a shape of n-fold symmetry, where n increases with the confinement. Electrostatic confinement restabilizes the circular droplet shape as the droplet size approaches the size of the cavity. Hydrodynamic confinement affects harmonic deformation modes of low n and is less important than the electrostatic confinement. The three phase coexistence region is not an equilibrium phase coexistence region, and material parameters such as $\mu_{LC/G}$, $\mu_{LE/G}$, and λ depend on the relative area fraction of the coexisting phases.

Acknowledgment. We thank G. Brezesinski for the use of the fluorescence microscope and Prof. H. Möhwald for generous support and stimulating discussion. This work was supported by the DFG priority program *wetting and structure formation at interfaces* and the Fonds der Deutschen Chemischen Industrie. T.M.F. thanks the Deutsche Forschungsgemeinschaft for providing a Heisenberg fellowship.

Appendix

Effective Line Tension and Confinement. In this section, we calculate the confined line tension. The electrostatic energy eq 20 of the droplet can be written as

$$\begin{aligned} W &= W_{LE,LE} + W_{LE,LC} + W_{LC,LC} \\ &= -\frac{\mu_{LE/G}^2}{2}\int_{-\pi}^{\pi}\int_{-\pi} d\varphi_1\, d\varphi_2 \times \\ &\frac{(r_1 r_2 + \dot r_1 \dot r_2)\cos(\varphi_1-\varphi_2) + (\dot r_1 r_2 - r_1 \dot r_2)\sin(\varphi_1-\varphi_2)}{\sqrt{r_1^2 + r_2^2 - 2r_1 r_2 \cos(\varphi_1-\varphi_2) + \Delta^2}} + \\ &\mu_{LE/G}\mu_{LC/G}\int_{-\pi}^{\pi}\int_{-\pi}^{\pi} d\varphi_1\, d\varphi_2 \times \\ &\frac{r_1 B\cos(\varphi_1-\varphi_2) + \dot r_1 B \sin(\varphi_1-\varphi_2)}{\sqrt{r_1^2 + B^2 - 2r_1 B\cos(\varphi_1-\varphi_2)}} - \\ &\frac{\mu_{LC/G}^2}{2}\int_{-\pi}^{\pi}\int_{-\pi}^{\pi} d\varphi_1\, d\varphi_2 \frac{B^2\cos(\varphi_1-\varphi_2)}{\sqrt{2B^2 - 2B^2\cos(\varphi_1-\varphi_2) + \Delta^2}} \end{aligned} \quad (A.1)$$

where the first term is the droplet self-interaction, the second term is the droplet surroundings interaction, and the third term is the self-interaction of the confining surroundings. The radii r_1 and r_2 are both given by eq 1 with the argument ϑ replaced by φ_1 and φ_2, respectively. The derivative of r with respect to its argument is denoted by $\dot r = dr/d\varphi$.

We wish to calculate the perturbation δW and δP under the constraint $\delta A = 0$. The latter constraints holds to the order ϵ^2 for the choice of deformation eq 1. The perturbation $\delta W_{LE,LE}$ has been calculated by Deutch and Low,[15] $\delta W_{LC,LC} = 0$, and the only remaining perturbation to be calculated is the interaction term $\delta W_{LC,LE}$.

Substituting $\varphi = \varphi_1 - \varphi_2$, introducing the abbreviation $\cos(\varphi) = (X(\varphi)^2 - B^2 - R^2)/2BR$, expanding $W_{LC,LE}$ to the order ϵ^2, and integrating over φ_1 leaves us with

$$\begin{aligned} W_{LC/LE} = \mu_{LE/G}\mu_{LC/G}\int_0^{2\pi} d\varphi\, \frac{\pi}{16X^5}\{-16(X^2 - B^2 - R^2)X^4 + \\ \epsilon^2[3X^6 + (B^2 - 3R^2)X^4 + (-7B^4 + 2B^2R^2 - 3R^4)X^2 + \\ (3B^6 - 3B^4R^2 - 3B^2R^4 + 3R^6)]\} \end{aligned} \quad (A.2)$$

The remaining integrals over φ are of the type

$$I_\nu = \frac{1}{4}\int_0^{2\pi} d\vartheta\, X^\nu(\varphi) = \int_0^{\pi/2} d\chi\, (p - q\sin^2\chi)^\nu \quad (A.3)$$

where $\chi = (\varphi - \pi)/2$, $p = (R + B)^2$, and $q = 4RB$.

Obviously, the integral obeys the relation

$$I_{\nu-1} = \frac{1}{\nu}\frac{\partial I_\nu}{\partial p} \quad (A.4)$$

For $\nu = {}^1/_2$ we find

$$I_{1/2} = p^{1/2}E(\sqrt{q/p}) = (B + R)E\left[\frac{2\sqrt{BR}}{B+R}\right] \quad (A.5)$$

Successively applying (A.4) to (A.5), we find

$$I_{-1/2} = \frac{1}{(B+R)} K\left[\frac{2\sqrt{BR}}{B+R}\right]$$

$$I_{-3/2} = \frac{1}{(B+R)(B-R)^2} E\left[\frac{2\sqrt{BR}}{B+R}\right]$$

$$I_{-5/2} = \frac{2}{3}\frac{B^2+R^2}{(B+R)^3(B-R)^4} E\left[\frac{2\sqrt{BR}}{B+R}\right] - \frac{1}{3}\frac{1}{(B+R)^3(B-R)^2} K\left[\frac{2\sqrt{BR}}{B+R}\right] \quad \text{(A.6)}$$

Inserting (A.5) and (A.6) into (A.2) and using $x = R/B$ yields

$$\delta W_{\mathrm{LC/LE}} = \epsilon^2 \pi R \mu_{\mathrm{LE/G}} \mu_{\mathrm{LC/G}} \frac{x}{1+x} \times \left\{\frac{1+x^2}{(1-x)^2} E\left[\frac{2\sqrt{x}}{1+x}\right] - K\left[\frac{2\sqrt{x}}{1+x}\right]\right\} \quad \text{(A.7)}$$

Finally, using

$$\delta P = 2\pi R \frac{\epsilon^2}{4}(n^2-1) \quad \text{(A.8)}$$

and the identities[23]

$$E\left[\frac{2\sqrt{x}}{1+x}\right] = \frac{1}{1+x}(2E(x) - (1-x^2)K(x))$$

$$K\left[\frac{2\sqrt{x}}{1+x}\right] = (1+x)K(x) \quad \text{(A.9)}$$

we find eqs 22, 23, and 26.

References and Notes

(1) Derjarguin, B. V.; Landau, L. *Acta Physicochim. URSS* **1941**, *14*, 633.

(2) Verwey, E. J. W.; Overbeek, J. Th. G. *Theory of Stability of Lyophobic Colloids*; Elsevier: Amsterdam, 1948.

(3) Horn, R. G.; Clarke, D. R.; Clarkson, M. T. *J. Mater. Res.* **1988**, *3*, 413.

(4) Horn, R. G.; Israelachvili, J. *J. Chem. Phys.* **1981**, *75*, 1403.

(5) Israelachvili, J. N.; Homola, A. M.; McGuiggan, P. M. *Science* **1988**, 240, 189.

(6) Hempel, E.; Hempel, G.; Hensel, A.; Schick, C.; Donth, E. *J. Phys. Chem. B* **2000**, *104*, 2460.

(7) Christenson, H. K. The long-range attraction between macroscopic hydrophobic surfaces. In *Approaches to wettability: theory and applications*; Schrader, M. E., Loeb, G., Eds.; Plenum Press: New York, 1992.

(8) Krech, M. *Phys. Rev. E* **1997**, *56*, 1642.

(9) McConnell, H. M. *Annu. Rev. Phys. Chem.* **1991**, *42*, 171.

(10) Lee, K. Y.; McConnell, H. M. *J. Phys. Chem.* **1993**, *97*, 9532.

(11) Steffen, P.; Heinig, P.; Wurlitzer, S.; Khattari, Z.; Fischer, Th. M. *J. Chem. Phys.* **2001**, *115*, 994.

(12) Stone, H. A.; McConnell, H. M. *Proc. R. Soc. London A* **1995**, *448*, 97.

(13) Happel, J.; Brenner, H. *Low Reynolds number hydrodynamics*; Martinus Nijhoff Publishers: The Hague, The Netherlands, 1983; p 77.

(14) Tranter, C. J. *Integral Transforms in mathematical physics*; Chapman and Hall: London, 1971; p 113.

(15) Deutch, J. M.; Low, F. E. *J. Phys. Chem.* **1992**, *96*, 7097.

(16) McConnell, H. M.; de Koker, R. *J. Phys. Chem.* **1992**, *96*, 7101.

(17) The line tension value stated for the case of negligible surface shear viscosity of the monolayer in ref 18 should be taken.

(18) Wurlitzer, S.; Steffen, P.; Fischer, Th. M. *J. Chem. Phys.* **2000**, *112*, 5915.

(19) Wurlitzer, S. *Statische und dynamische Eigenschaften von Mikrostrukturen in Langmuir Monolayern*, Dissertation, University of Leipzig, 2001.

(20) This value of the line tension has been chosen, such that the first 25 modes are unstable, which is in agreement with the experiment, whereas dipole densities are those determined by the experiment. Other choices for the line tension and dipole densities would change the quantitative not the qualitative behavior.

(21) *Landolt Börnstein IV/1*, 6th ed.; Springer: Berlin, Germany, 1955; pp 600 and 613.

(22) Schwartz, D. K.; Tsao, M. W.; Knobler, C. M. *J. Chem. Phys.* **1994**, *101*, 8258.

(23) Gradstein, I. S.; Ryshik, I. M. *Tables of series, produts and integrals*; Harri Deutsch: Frankfurt, Germany, 1981; Vol 2, No. 8.126.